ACS APPLIED MATERIALS & INTERFACES

www.acsami.org

Research Article

A Label-Free Diamond Microfluidic DNA Sensor Based on Active Nitrogen-Vacancy Center Charge State Control

Marie Krečmarová, Michal Gulka, Thijs Vandenryt, Jaroslav Hrubý, Ladislav Fekete, Pavel Hubík, Andrew Taylor, Vincent Mortet, Ronald Thoelen, Emilie Bourgeois, and Miloš Nesládek*

Cite This: *ACS Appl. Mater. Interfaces* 2021, 13, 18500–18510

Read Online

ACCESS | Metrics & More | Article Recommendations | Supporting Information

ABSTRACT: We propose a label-free biosensor concept based on the charge state manipulation of nitrogen-vacancy (NV) quantum color centers in diamond, combined with an electrochemical microfluidic flow cell sensor, constructed on boron-doped diamond. This device can be set at a defined electrochemical potential, locking onto the particular chemical reaction, whilst the NV center provides the sensing function. The NV charge state occupation is initially prepared by applying a bias voltage on a gate electrode and then subsequently altered by exposure to detected charged molecules. We demonstrate the functionality of the device by performing label-free optical detection of DNA molecules. In this experiment, a monolayer of strongly cationic charged polymer polyethylenimine is used to shift the charge state of near surface NV centers from negatively charged NV^- to neutral NV^0 or dark positively charged NV^+. Immobilization of negatively charged DNA molecules on the surface of the sensor restores the NV centers charge state back to the negatively charged NV^-, which is detected using confocal photoluminescence microscopy. Biochemical reactions in the microfluidic channel are characterized by electrochemical impedance spectroscopy. The use of the developed electrochemical device can also be extended to nuclear magnetic resonance spin sensing.

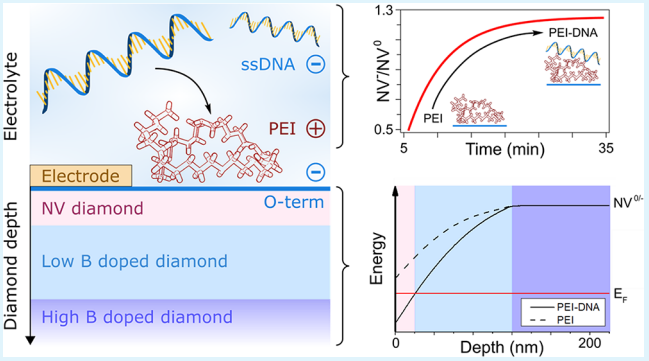

KEYWORDS: *nitrogen-vacancy center, diamond, biosensor, microfluidic, DNA chip*

1. INTRODUCTION

DNA diagnostics have become one of the major biochemical analytical tool of today. Further challenges lay in the development of novel sensing principles, which can detect significantly reduced volumes of analytes and operate label-free with an enhanced sensitivity or readout speed. Artificial diamond attracts significant attention for biosensing applications thanks to its unique combination of physical and chemical properties, which can be tuned during fabrication, with key advantages such as biocompatibility and non-toxicity.[1] Diamond electrodes, fabricated from boron-doped diamond (BDD) prepared by chemical vapor deposition (CVD) growth,[2] have demonstrated excellent electrochemical properties such as low electrochemical background currents or a large potential window,[3] allowing detection of a wide range of chemical species without being limited by the water splitting potential. The conductivity of such electrodes can be tuned by varying the boron acceptor concentration incorporated during the diamond growth. BDD layers can range from semiconductive (from a boron concentration of $\sim 10^{16}$ cm^{-3})[4] to metallic (from a boron concentration of $\sim 2 \times 10^{20}$ cm^{-3}).[5] Sensors based on conductive p-type BDD were explored widely in various proof-of-principle studies including pH sensing,[6] electrochemical detection of biomolecules (glucose,[7] DNA,[8] and viruses[9]), or recording of neural activity.[10] Another important method employed for advanced molecular sensing is based on luminescence and spin properties of point defects in the diamond lattice, known as color centres.[11,12] Among many known color centers, the nitrogen-vacancy (NV) center is one of the most studied, allowing sensing at room temperature. The NV color center, acting as a quantum spin probe, has been used in the breakthrough achievement of single molecular imaging. Using quantum techniques, detection of single proton[13] or single electron spins[14] in spin-labeled single proteins,[15] has been reported.[16−21]

The NV center consists of a substitutional nitrogen atom adjacent to a vacancy in the diamond lattice (see Figure 1). It can exhibit negative NV^- and neutral NV^0 charge states with a zero-phonon line (ZPL) at 637 and 575 nm, respectively, or a

Received: January 18, 2021
Accepted: March 30, 2021
Published: April 13, 2021

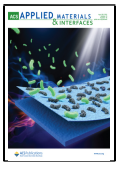

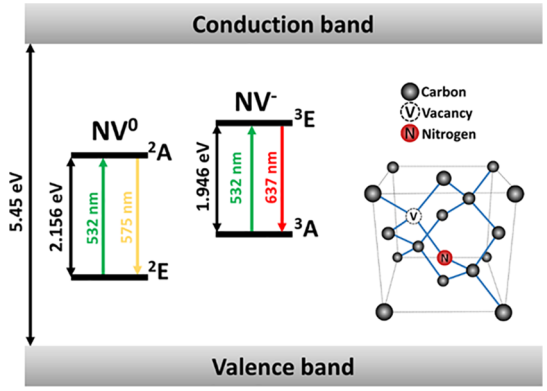

Figure 1. (a) Energy levels of the NV^- center (triplet ^3A ground state (GS) and ^3E excited state (ES)) and the NV^0 center (doublet ^2E GS and ^2A ES), with an excitation wavelength of 532 nm (green arrows) and zero-phonon line emission at 575 nm for the NV^0 center (yellow arrow) and 637 nm for the NV^- center (red arrow). Inset: scheme of the NV center showing a substitutional nitrogen atom forming a complex with a vacancy in diamond lattice.

positive dark NV^+ charge state.[22−25] The inner conversion between the $NV^{0/+/-}$ charge states can be achieved by manipulation with the Fermi level position. This principle of NV center charge switching was pioneered in our works applied to nanodiamond (ND) particles.[26−28] In parallel, the NV charge sensing principle was used for monitoring changes between hydrogen- and oxygen-terminated surfaces[29,30] on single crystal diamond, the effect of an external electrical control,[25,31−35] and very recently the influence of electrochemical potential on ND particles.[36] These results show that switching of the charge state of NV centers has a vast potential for the detection of charged molecules.[37] The devices used in these different studies were based solely on un-doped diamond as the negatively charged NV^- state of the NV center cannot exist in BDD due to the Fermi level (E_F) pinning close to the valence band edge of diamond E_v. However, in our preliminary work,[38] we were able to engineer NV^- charge states in device structures using a combination of B-doped and un-doped NV-containing diamond layers, merging advantages of both the electrochemical sensing using BDD and NV sensing using un-doped (or N-doped) diamond. This is achieved by using an ultrathin un-doped diamond layer hosting the NV centers, deposited on a BDD layer.

In the present work, we develop this concept and establish, in detail, the sensing capabilities of our scheme, measure the time dependent detection sensitivity, and demonstrate the electrochemically controlled NV center charge state switching for DNA detection. It is important to note that this sensing principle can be used for detection of any molecule carrying an electrical charge, which interacts with the diamond sensor surface. The NV charge state sensor device functionality is achieved by a combination of BDD electrodes with the NV-doped diamond layer. It allows for setting the device at electrochemical potentials with respect to the electrochemical potential of the analyte, within the diamond electrochemical window.[39] In addition to PL detection, the device can be used as an NV electron spin sensor, being usable for NMR detection[13] at various chemical potentials. Moreover, the presented label-free detection method has a range of further potential applications in medicine, drug development industry, or forensics.

The functionality of the fabricated structure for the active NV charge state control and sensing was first verified by applying a voltage on the gate electrode of the device whilst monitoring NV photoluminescence under various gate bias conditions. Then, DNA molecules were attached to the diamond surface functionalized with a cationic polymer, polyethylenimine (PEI),[37] and label-free optical detection of

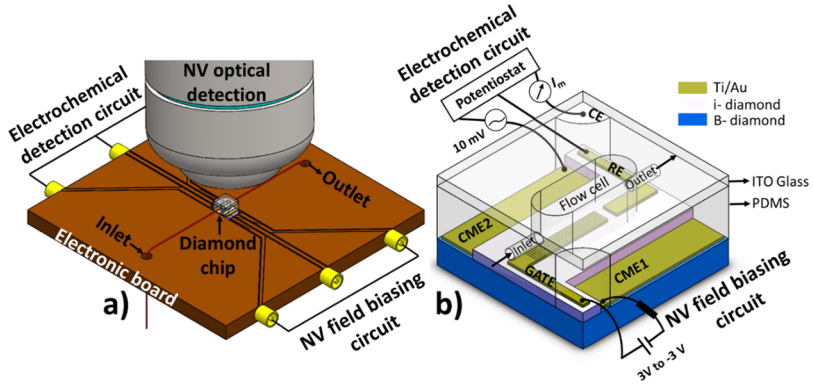

Figure 2. (a) Scheme of sensor arrangement showing the diamond chip covered with a microfluidic flow cell, embedded, and electrically connected to an electronic board. PL signal is collected using a long-distance objective confocal microscope through micro-holes fabricated in the gate electrode of the flow cell. (b) Detailed schematics of the diamond chip containing a BDD layer overgrown with a thin layer of un-doped diamond with NV centers covered with a PDMS flow cell and an ITO coated glass slide on top. Diamond is equipped with coplanar Ti/Au electrodes connected to two electronic circuits, one for electrochemical detection and the second one for NV charge state manipulation. The sensor consists of two electrodes on BDD: complementary electrode no. 1 (CME1, NV charge state manipulation by field biasing circuit) and complementary electrode no. 2 (CME2, electrochemical detection circuit), two electrodes on un-doped diamond with NVs: reference electrode (RE, electrochemical detection circuit) and gate electrode (GATE, NV charge state manipulation circuit), and one electrode on an ITO coated glass slide acting as a counter electrode (CE, electrochemical detection circuit). The GATE, RE, and CE electrodes are exposed to the electrolyte, whereas the CME1 and the CME2 electrodes are isolated from the electrolyte. For EIS measurements, a 10 mV AC voltage was applied between the CME2 and CE electrodes, the RE was grounded, and other electrodes had a floating ground potential. Active control of the NV center charge state is achieved by an external electric field applied onto the GATE against CME1 and thus tuned for the highest sensitivity to the detected charged molecules (i.e., DNA). The RE electrode had a floating ground potential, and CME2 and CE were grounded. The consequent change in PL is detected by confocal microscopy. The details are discussed in the Supporting Information.

https://doi.org/10.1021/acsami.1c01118
ACS Appl. Mater. Interfaces 2021, 13, 18500−18510

Table 1. Growth Parameters of Diamond Layers

diamond layers	CH_4 concentration (%)	B/C ratio (ppm)	microwave power (W)	working pressure (mbar)	substrate temperature (°C)
highly doped BDD	1	6000	700	100	1100
low-doped BDD	2	1	750	93	890
NV-doped layer	0.4	0	900	93	940

DNA molecules based on the manipulation of NV charge states was demonstrated. At the same time, we used the device for label-free electrochemical DNA detection based on B-doped electrodes. The principle and operation of the device are further explained in the text.

2. MATERIALS AND METHODS

The essential part of the described device is a nanometer-thin diamond layer, which contains stable NV centers used for charge sensing (both NV^0 and NV^-), and an optimally doped BDD electrode for electrochemical control. This design is not trivial since, as mentioned above, the NV^- center charge state is unstable in BDD (p-type). Therefore, thickness and NV concentration of the few-nanometer thin diamond layer, as well as B concentration in the BDD layer, are extremely important parameters and we optimize these quantities by modeling (see Supporting Information, Figure S3). To use the band bending methodology, the diamond device is equipped with electrodes arranged in a field-effect transistor (FET)-like configuration, allowing one to manipulate the NV center charge state by an electric field applied to the gate. The diamond device is covered by a microfluidic flow cell made of polydimethylsiloxane (PDMS) and an indium tin oxide (ITO) glass slide. The NV center charge state is detected by confocal photoluminescence (PL) microscopy as a response to charged species produced by biochemical reactions happening in close proximity to the diamond surface and being trapped on the surface. The device can be also used at the same time for electrochemical impedance spectroscopy (EIS) or cyclic voltammetry (CV) electrochemical sensing techniques. The device design is depicted in Figure 2a,b.

2.1. Fabrication of the Device. Metallically conductive highly doped BDD homoepitaxy layers were grown on polished Sumitomo Electric Hartmetall GmbH (100) oriented single crystal diamonds (3.2 × 3.2 mm surface area) using a Seki Technotron AX5010 CVD system and a hydrogen-rich gas with diborane used as the B dopant. Growth parameters are summarized in Table 1. The diamond surfaces were polished after the growth of the layers to obtain a surface roughness (Rms) of <1 nm. Two fabricated BDD layers associated with active NV layers (BDD−NV) were used. These samples are denoted as 1 and 2. Compared to sample 1 (see Figure S1a,c in the Supporting Information), sample 2 (see Figure 1b,d in the Supporting Information) contains an additional low-doped BDD interlayer between the highly doped BDD and the un-doped diamond layer with NV centers. Subsequently, for both samples, the as as-grown and polished BDD layer was protected from the next un-doped diamond CVD growth step by thin titanium layers, which can be also used as complementary electrodes and were later further metalized for this purpose. In the case of sample 2, the uncoated, i.e., Ti-free, area of the metallically conductive BDD layer was overgrown by a low-doped BDD diamond interlayer using an Astex AX6500 CVD system with trimethylboron as the B dopant in hydrogen gas and growth parameters depicted in Table 1. On the Ti-free part of the metallically conductive BDD layer (sample 1) and on the low-doped BDD layer (sample 2), another nominally un-doped diamond thin film was grown in hydrogen gas, using the growth parameters shown in Table 1. NV centers were incorporated in these layers from residual nitrogen present in the chamber. Sample 1's structure thus consists of a ∼20 μm BDD layer and a ∼15 nm unintentionally doped diamond film with NV centers on top, whilst sample 2 consists of a ∼20 μm BDD layer, a ∼100 nm low-doped BDD interlayer, and a ∼20 nm unintentionally doped diamond film with NV centers on top (see Figure S1 in the Supporting Information).

The diamond surface of both un-doped layers was oxygen-terminated via plasma exposure in a Technics PE-IIA plasma system (power of 50 W, working pressure of 1 mbar, and duration of 2 min). Then, both samples were metalized by fabrication of four titanium/gold electrodes (see Figure 2b). Two areas on metallically conductive BDD (denoted as complementary electrodes no. 1 and no. 2) and 2 areas on the un-doped diamond layer (denoted as gate and reference electrodes) were fabricated. The ohmic titanium/gold (Ti/Au = 20/80 nm) contacts were fabricated by classical photolithography including metal evaporation and wet etching followed by thermal annealing. A PDMS flow cell was fabricated by creation of a microchannel in a PDMS film followed by laser cutting to the desired design. The PDMS flow cell was placed on the diamond substrate, mounted on an electronic board, and covered with an ITO coated glass, serving as a counter electrode on top of the microfluidic channel. The total thickness of the PDMS/ITO structure is 2.5 mm, which is smaller than the working distance of the objective utilized for confocal microscopy (WD = 3.4 mm). The volume of the flow cell is ∼20 μL. The shallow lying NV centers are optically accessible through openings in a gate deposited on the NV-doped layer. The scheme of the complete sensing device chip is depicted in Figure 2 (see also Supporting Information, Figure S1).

2.2. DNA Sample Preparation. A solution of PEI 50% w/v in H_2O purchased from Sigma-Aldrich was first diluted with Milli-Q water to a final concentration of 0.3% w/v and ultra-sonicated for 30 min. The oxygen-terminated diamond sensor was immersed into the solution for 8 h. During immersion, PEI molecules were electrostatically attracted to the negative oxygen-terminated diamond surface.[10,37] The diamond surface was then rinsed with Milli-Q water to remove un-adhered PEI molecules and dried with a nitrogen gun. For DNA detection experiments, NH_2-terminated single-stranded DNA (ssDNA) oligo-molecules with 23 bases 5′-/5AmMC6/TTT TTA ATT AAA GCT CGC CAT CA purchased from Integrated DNA Technologies, BVBA, were used. Dry DNA molecules were diluted in Milli-Q water up to concentrations of 0.1, 1, 10, and 100 μM and vortexed using a VWR Analog Vortex Mixer (300 rpm for 1 min). A LSPone - Laboratory syringe micro-pump was used for filling the microfluidic sensor flow cell. For on/off mode DNA sensing, the flow cell was first pumped with a DNA solution (0.1−100 μM) and kept filled for 1 h for sedimentation of DNA molecules onto the PEI-terminated diamond surface. Then, the solution was replaced with phosphate-buffered saline (PBS) electrolyte for further measurements and also to remove un-adhered DNA molecules from the PEI layer. In the case of time-dependent sensing experiments, water solutions of DNA molecules with concentrations of 10 and 100 μM were used without further flushing of the PBS electrolyte.

2.3. Electrochemical Impedance Spectroscopy. EIS measurements were carried out using a Hewlett Packard 4248 Precision LCR meter. Impedance was measured with a 10 mV AC voltage applied to the flow cell at room temperature. BupH phosphate PBS with pH 7.2 was used as an electrolyte, which was ultra-sonicated for 5 min before filling the flow cell to prevent bubble formation. Impedance was measured for 151 frequencies of AC voltage in a range from 1 Hz to 100 kHz.

2.4. Photoluminescence Measurements. PL experiments were carried out using a lab-built confocal microscope. NV centers were excited by a green 532 nm CW Gem laser from Laser Quantum with a laser power of 8 mW, directed onto the sample by Gaussian beam optics and a long working distance M Plan Semi-Apochromat Olympus objective (N.A. = 0.8, WD = 3.4 mm). PL maps were detected using an Excelitas single photon counter. PL two- and three-dimensional maps were plotted using Matlab software from

https://doi.org/10.1021/acsami.1c01118
ACS Appl. Mater. Interfaces 2021, 13, 18500−18510

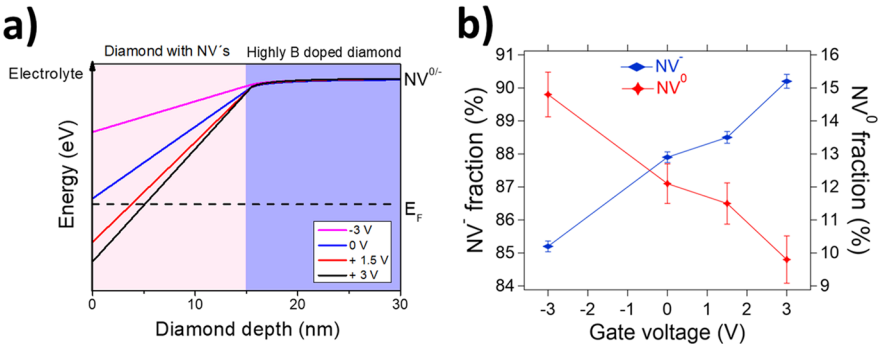

Figure 3. (a) Sample 1, band bending simulations of NV^- center transition energy level positions with respect to the sample depth for various gate voltages (ranging from −3 to +3 V). A nitrogen concentration of 10^{15} cm^{-3} in the un-doped diamond top layer with oxygen-terminated surfaces was used for the simulations. (b) NV^- and NV^0 fraction extracted from averaged PL spectra measured on sample 1 for different gate voltages (−3 to +3 V). The NV^- and NV^0 fraction was calculated by Lorentzian peak fit (see Section 2) of the measured PL spectra, showing the increase in the NV^- center occupation with application of a positive gate voltage.

MathWorks.[40] PL spectra measurements were carried out using a monochromator combined with an avalanche photodiode (APD) photodetector (for active control of the NV charge state) or by a spectrometer associated with a charge-coupled device (CCD) camera (for DNA detection). To extract the NV^-/NV^0 ratio from the recorded PL spectra, we first fitted the ZPL and phonon side bands forming the single NV^- and NV^0 PL spectra[41] using Lorentzian functions. The measured PL spectra were then accordingly fitted. The fraction of the signal resulting from NV^- (NV^0) PL emission was established by integrating the intensity of the fitting peaks related to NV^- (NV^0). Time-dependent NV PL measurements were recorded at spots where micro-holes were fabricated through the gate. The measurements for DNA concentrations of both 10 and 100 μM, as a function of time, were executed up to 34 min after DNA bonding.

2.5. Simulations and Modeling. Band bending of electron energy levels of sample structures 1 and 2 with different surface functionalization and applied gate voltages was simulated using AMPS-1D software[42] (Analysis of Microelectronic and Photonic Structures) using numerical solutions of the Poisson's equation. For the simulation, we used the following parameters: a highly doped BDD bottom layer with [acceptor] = 10^{21} cm^{-3}, low-doped BDD interlayer with [acceptor] = 10^{17} cm^{-3}, and un-doped N layer on top with [donor] = 10^{15} cm^{-3} or [donor] = 10^{18} cm^{-3} for various applied voltages on the device. Electrical circuit parameters were determined by fitting the impedance data to the equivalent circuit (see the Supporting Information) using "Zview" software from Scribner Associates.[43]

2.6. Sensing Devices Operation. The sensing device is depicted in Figure 2. The PDMS microfluidic device structure has two circular cut-outs on the sides to enable wire bonding of four electrodes on the corners of the diamond chip. Two main electrical detection circuits are used (see Figure 2b; for more details, see Figure S2 in the Supporting Information) with the main functions of active control of the NV center charge states (Figure S2a in Supporting Information) and electrochemical detection (Figure S2b in Supporting Information).

Electrical control of the NV charge state was performed by application of a voltage from −3 to +3 V to the gate electrode on un-doped diamond with NV centers against the complementary electrode no. 1 (CME1) on BDD. PL from NV centers was recorded through holes micro-fabricated in the gate electrode (Figure 2 and Figure S7b in Supporting Information for more details). EIS was carried out using a three-electrode terminal system including complementary electrode no. 2 (CME2) on BDD, reference electrode (RE) on un-doped diamond, and counter electrode (CE) on the ITO glass slide covering the flow cell. For EIS, an AC voltage was applied over a range of frequencies. Electrodes on the BDD surface were isolated from the electrolyte by constructing a PMDS microfluidic cell, as discussed above. The RE, gate, and CE were immersed in the liquid electrolyte.

3. RESULTS AND DISCUSSIONS

3.1. Active Control of the NV Charge State. The band bending profile of both device (sample 1 and sample 2) structures immersed in electrolyte solution was modeled numerically (Figure S3a,b in the Supporting Information). In the modeling, we assumed an oxygen-terminated un-doped diamond surface with the highest occupation of negatively charged NV centers, as confirmed by our previous research.[29,38] Modeling suggested that, in the case of sample 1, without the application of any voltage on the gate electrode, the NV^- charge state is unstable as the metallically doped BDD layer pins the Fermi level close to the valence band and NV^- is inhomogenously depleted to the NV^0 charge state (see Figure S3a in the Supporting Information). On the other hand, the presence of a low-doped (1 ppm) BDD interlayer in sample 2 stabilizes the Fermi level position above the NV^- defect level (see Figure S3b in the Supporting Information). The results from the band bending modeling were confirmed by PL measurements on oxygen- terminated surfaces of samples 1 and 2, showing a higher emission for NV^0-related PL for sample 1 and stronger NV^--related PL for sample 2 (not shown). The applied voltage then enables precise control of the E_F to produce either NV^- or NV^0 charged states.[44]

To study the NV charge state in the un-doped diamond layer under various voltages, we controlled the band bending profile by applying a bias voltage from −3 to +3 V on the gate electrode against the CME1. First, we used sample 1. In this case, the NV centers were mainly in the NV^0 charge state even after oxygen termination. Modeling of band bending gives a value of 2.7 × 10^6 V/cm for the electric field in the un-doped layer for a maximum applied voltage of +3 V (~10 times lower than the breakdown voltage threshold of diamond). The simulated band bending profile of the NV^- center level under different gate voltages is plotted in Figure 3a, assuming the nitrogen concentration of 10^{15} cm^{-3} in the un-doped layer. A negative gate voltage (−3 V) shifts the bands upward against the Fermi level position and thus destabilizes the NV^- charge state in the whole depth (~15 nm) of the un-doped film. For a positive gate voltage (+1.5 and +3 V), bands are shifted downward against the Fermi level and the negative charge state of NV center is stabilized. According to our modeling, under a voltage of +3 V, the Fermi level intersects the NV^- defect level at a sample depth of ~5 nm and the NV^0 defect level (not shown in Figure 3a) at a depth of ~13 nm. This means that

https://doi.org/10.1021/acsami.1c01118
ACS Appl. Mater. Interfaces 2021, 13, 18500−18510

only deeper NV centers, laying close (up to ~2 nm) to the BDD (B/C 6000 ppm) layer, are in the non-active NV^+ charge states. We also simulated the band bending profile of the NV^- center level of sample 1, which has a 1000× higher nitrogen concentration of 10^{18} cm^{-3} (see Figure S4e in the Supporting Information). However, such an increase in the nitrogen concentration does not lead to a dramatic change in the band bending profile, showing a similar trend as for lower concentrations. This is because the metallically B-doped BDD layer pins the Fermi level position and N is a deep donor. The position of the NV^0 and NV^- ground states (GS) and excited states (ES) has been also discussed in detail in refs 11, 23, 29. By precisely tuning the applied voltage, the NV charge state can thus be switched.[32]

To confirm experimentally the band bending modeling results, we measured NV charge state switching using PL spectroscopy. We monitored the influence of the gate voltage on the NV center charge state of sample 1 at different positions close to the gate electrode. The measured average NV PL spectra were fitted to obtain NV^- and NV^0 fractions in the total signal, and these fractions were plotted as a function of the gate voltage (Figure 3b). When a +1.5 V voltage is applied, NV^- PL increases compared to an unbiased measurement at 0 V. This effect is even more pronounced for a higher voltage of +3 V as NV^- PL increases significantly. As expected, application of a −3 V negative voltage leads to the opposite effect. The NV^-/NV^0 ratio decreases as the NVs are converted to their neutral state. These results are consistent with band bending modeling (Figure 3a). To quantify this effect on a larger scale, we examined the voltage effect by PL mapping, performed with a long-pass spectral filter to enable detection of only the PL signal associated with NV^-. Figure 4 and Figure S4a–c in the Supporting Information show PL intensity in 2D and difference 3D maps for bias voltages of −3 and +3 V. These results show an increase in NV^- PL for a bias voltage of +3 V, confirming that more NV centers are changed to the

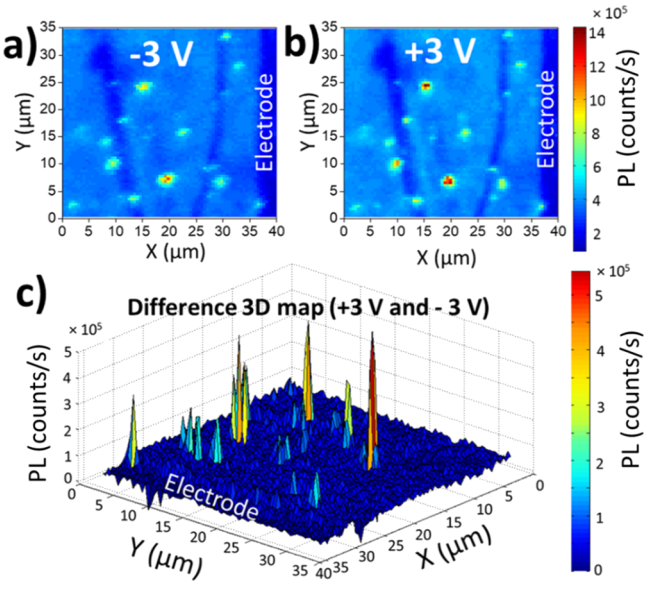

Figure 4. PL intensity (a, b) 2D maps and (c) differential 3D map of sample 1 with (a) −3 V and (b) +3 V gate voltages. Measurements were performed with a long-pass spectral filter with cut-on wavelength at 650 nm to remove NV^0 PL, showing a higher number of active NV^- centers for a positive voltage.

NV^- charge state. When a negative voltage of −3 V is applied, the same spots become darker, in agreement with the band bending modeling (Figure 3a). Switching between the NV^- and NV^0 charge state occupation by voltage control (between +3 and −3 V) is well reproducible, and we did not observe any hysteresis. As a conclusion, we confirmed that we could achieve electrically controlled NV charge switching in structures consisting of a stacked NV-doped layer on top of the p-type boron-doped diamond.

3.2. DNA Detection by a BDD-NV Sensor. By combination of NV charge state detection with EIS in our microfluidic sensing device, we aim to develop sensitive chemical detectors in which we can set the electrode at a predefined electrochemical potential and, at this potential, sense charged molecules. Such a device would have use, for example, for the detection of species, which are produced by chemical reactions at specific electrolyte potentials. This principle is demonstrated here for the detection of DNA molecules noncovalently adsorbed on a PEI-functionalized diamond surface. In this case, the originally positively charged PEI surface is compensated by negatively charged DNA molecules, changing the band bending at the diamond surface and consequently the charge state, and therefore the PL emission, of shallow NV centers.

To verify charge state manipulation in the electrolyte, we have performed band bending modeling for both samples 1 and 2. The band bending was simulated for two different nitrogen donor concentrations in the NV-containing upper layer. A lower concentration of 10^{15} cm^{-3} corresponds to samples used in this experiment, whereas a higher concentration of 10^{18} cm^{-3} was simulated to predict further improvements of the sensor sensitivity (higher PL from NV centers). From the modeling, it turns out that sample 2, with an additional low-doped BDD layer, is more suitable to be used as a sensor as NV centers can be tuned to be positive or negative by the application of PEI or DNA-PEI layers, respectively. The results of the band bending modeling of sample 2 are shown in Figure S5 in the Supporting Information for [donor] = 10^{15} cm^{-3} and in Figure S6 in the Supporting Information for [donor] = 10^{18} cm^{-3}. PEI functionalization strongly depletes the NV^- charge state at the surface by Fermi level pinning. This NV^- depletion holds even for a positive gate voltage applied up to +1 V (Figures S5c and S6c in the Supporting Information). Upon DNA attachment, NV^0 centers are converted to the NV^- charge state for simulated gate voltages from 0 to +3 V (Figures S5d and S6d in the Supporting Information). Figure 5 summarizes the results of band bending simulations of the NV^- center transition energy level at a 0 V gate voltage for PEI and PEI-DNA surface functionalization of sample 2 immersed in electrolyte solution for both concentrations of donors in the top layer with NV centers [N = 10^{15} cm^{-3}, N = 10^{18} cm^{-3}]. The Fermi level is positioned below the NV^- GS level for PEI functionalization and above the NV^- GS level after DNA attachment for both simulated nitrogen concentrations. In the case of sample 2 used in this experiment with a lower nitrogen concentration, the Fermi level is positioned more centrally between the NV^- GS level for PEI and DNA functionalization. Since this is an optimal state, we did not apply a gate voltage for DNA detection. The band bending can be adapted by application of voltage for various N doping levels.

First, we used the electrochemical function of our BDD-NV sensor and measured EIS to characterize DNA attachment on

https://doi.org/10.1021/acsami.1c01118
ACS Appl. Mater. Interfaces 2021, 13, 18500−18510

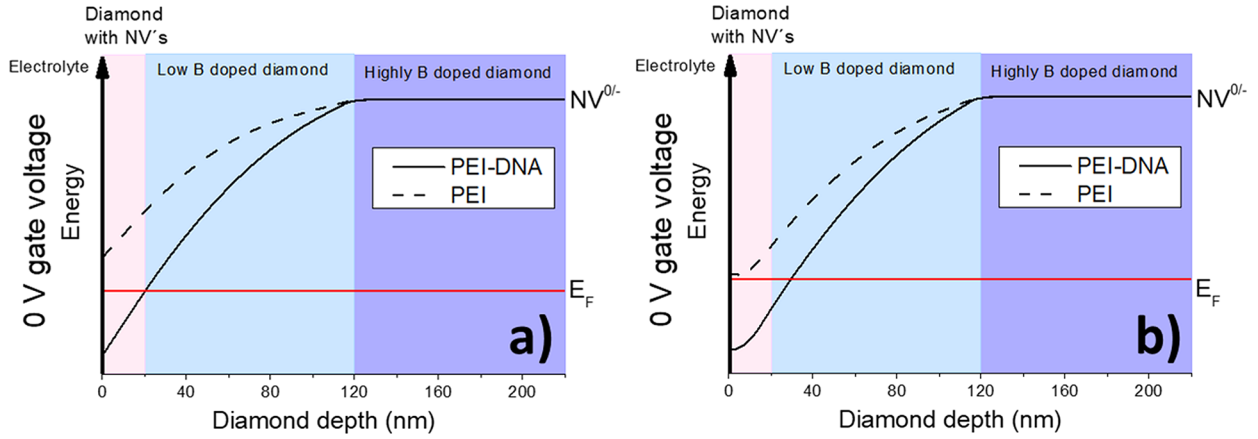

Figure 5. Band bending simulation (sample 2) of the NV^- center transition energy level at a 0 V gate voltage for PEI and PEI-DNA surface functionalization with a nitrogen donor concentration in the un-doped diamond layer containing NV centers of (a) 10^{15} cm^{-3} and (b) 10^{18} cm^{-3}. The plots show the restoration of the NV^- charge state at the surface of the diamond chip in the presence of DNA, where the Fermi energy level is positioned above the energy of the NV^- state.

the diamond chip surface. The surface of sample 2 was covered with a monolayer of strongly cationic charged PEI polymer. The presence of PEI molecules on the diamond charged surface was confirmed in our previous work[45] by X-ray photoelectron spectroscopy (XPS). ssDNA with concentrations ranging from 0.1 to 100 μM were used as target molecules. DNA molecules flowing in the microfluidic channel were electrostatically attracted onto the positively charged PEI coated diamond surface, and those molecules, which were not strongly immobilized, were flushed away. A Nyquist plot of the imaginary part of impedance (−Im|Z|) as a function of the real part of impedance (Re|Z|) is depicted for different DNA concentrations (0−100 μM) in Figure 6a,b. It follows that the

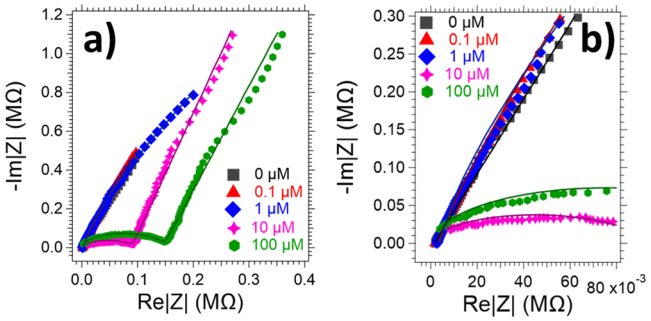

Figure 6. (a) Nyquist plot and (b) zoom of the Nyquist plot showing the real and imaginary part of the complex impedance for PEI and PEI-DNA functionalized diamond surfaces (measured on sample 2) with DNA concentrations varying from 0 to 100 μM. Symbols represent experimental data, and lines represent fitted values.

Nyquist plot presents an almost linear trend for DNA concentrations up to 1 μM and only slightly changes when the DNA concentration is increased from 0.1 μM to 1 μM. On the other hand, at higher DNA concentrations, the Nyquist plot consists of a semicircle followed by rising characteristics.

Impedance data were fitted using an equivalent circuit (see Figure S8a in the Supporting Information). The model circuit consists of resistance of the electrolyte R_S, in series on the one hand with a parallel combination of double layer (dl) capacitance C_{dl} and resistance R_{dl} and on the other hand with another parallel combination of charge space region (scr) capacitance C_{scr} and resistance R_{scr}. This equivalent circuit provided the best fit to our experimental data. All fitted parameters are shown in Figure S8b in the Supporting Information. The key monitored parameter is the resistance R_{dl} of the interface between the diamond chip surface and the surrounding electrolyte (see Figure S8a in the Supporting Information). Figure S8c shows the dependence of R_{dl} on DNA concentration ranging from 0.1 to 100 μM. The R_{dl} for the minimum DNA concentration of 0.1 μM is almost unchanged (9 kΩ) in comparison to the bare diamond surface without immobilization of any DNA molecule (8 kΩ). The R_{dl} starts to increase when the DNA concentration is changed to 1 μM (17 kΩ) and then increases more dramatically for DNA concentrations equal to 10 μM (468 kΩ). Finally, it saturates at the highest DNA concentration of 100 μM (531 kΩ). It therefore follows from our measurements that the detection limit of the electrochemical sensor is about 1 μM DNA. The results of EIS detection are consistent with the literature[45−47] and confirm that DNA molecules (≥1 μM) were successfully bound to the PEI-terminated diamond surface.

After verification of the principle of DNA attachment, we used NV PL to monitor DNA immobilization onto the PEI functionalized diamond surfaces (sample 2) through holes in the gate electrode and compare with the EIS results. The bias voltage on the gate electrode was set to 0 V, which corresponds to an intermediate position of the Fermi level E_F between PEI and PEI-DNA energy levels on the diamond surface according to band bending calculations (Figure 5a). In order to have a better understanding of the behavior of the NV center charge state and to obtain the highest sensor response, first we monitored NV PL at two different positions as a function of time during DNA bonding (i.e., when the DNA flow was introduced to the microfluidic channel). Considering EIS measurements, we used DNA concentrations of 10 and 100 μM. The measured NV PL spectra were fitted (see Section 2) to obtain the NV^-/NV^0 ratio and plotted as a function of DNA bonding time (over 35 min). Figure 7 represents the time-dependent variation of the NV^-/NV^0 ratio for DNA concentrations of 10 μM (Figure 7a) and 100 μM (Figure 7b) measured at two different positions. For 10 μM, the NV^-/NV^0 ratio increases throughout the full measurement time, whilst for the 100 μM concentration at the beginning of measurement (15 min), the NV^-/NV^0 ratio increases monotonically and saturates after 17 min. It should be noted

https://doi.org/10.1021/acsami.1c01118
ACS Appl. Mater. Interfaces 2021, 13, 18500−18510

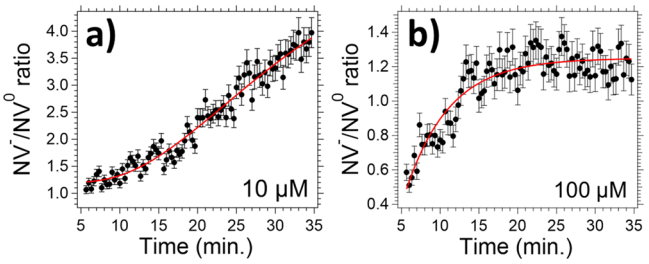

Figure 7. (a) Time-dependent NV^-/NV^0 ratio monitored during the continuous DNA attachment on a PEI-terminated diamond surface (sample 2), measured at two different points for DNA concentrations of (a) 10 μM and (b) 100 μM. Black circles represent NV^-/NV^0 ratio, determined by Lorentzian peak fitting of NV^- and NV^0 PL (ZPL and side bands), and red lines represent their trends.

that the saturation of the NV^-/NV^0 ratio for the 10 μM DNA concentration was observed as well after approximately 45 min (not shown here).

Further on, we investigated NV charge state DNA detection by PL monitoring of 123 different spots through gate micro-holes on the diamond surface. For this study, we used the maximal DNA concentration of 100 μM, showing the highest response. Unlike the case of time-dependent measurements, here the NV charge state was monitored before and after DNA bonding on the PEI-terminated diamond surface. PL intensity maps of the diamond surface monitored through the micro-holes (light blue circles) on the gate electrode in high magnification for 2D and differential 3D case are plotted in Figure 8 (other measured micro-holes are presented in Supporting Information, Figure S7c,d). The collected PL intensity differs for PEI (Figure 8a,d) and PEI-DNA surface functionalization (Figure 8b,e). When negative DNA molecules are attracted to the positive PEI functionalized diamond surface, the intensity of NV^--related photoluminescence increases (Figure 8c,f). In good agreement with our band bending simulations, this can be explained by an increase in NV^- center population as a result of band bending variations originating from interactions of electrical charge with immobilized DNA molecules (see Supporting Information, Figure S5). Indeed, whilst NV centers are mainly in the NV^0 charge state with PEI termination, they are switched to the NV^- charge state after PEI-DNA functionalization. Averaged NV PL spectra of 123 spots in micro-holes before and after DNA attachment are shown in Figure 9a. As expected, the charge state of NV centers varies considerably with diamond surface functionalization. By fitting the averaged spectra, we calculated the proportion of NV^0 and NV^- PL with PEI and PEI-DNA surface functionalization. For fitting of the spectra, we used the integrated peak intensity of ZPL and phonon sidebands corresponding to single NV^0 and NV^- centres.[41] Specifically, the peak at 575 nm and its side band around 610 nm for the NV^0 contribution ZPL and the peak located at 637 nm and its side bands around 660 and 680 nm for the NV^- contribution ZPL were used, respectively. PEI functionalization tunes NV centers to NV^0 with a calculated contribution of 49.9% for NV^0 PL and 50.1% for NV^- PL for the average spectrum. After DNA attachment, the calculated NV^- contribution significantly increases (up to 71%) due to NV switching to the negative charge state in the presence of the

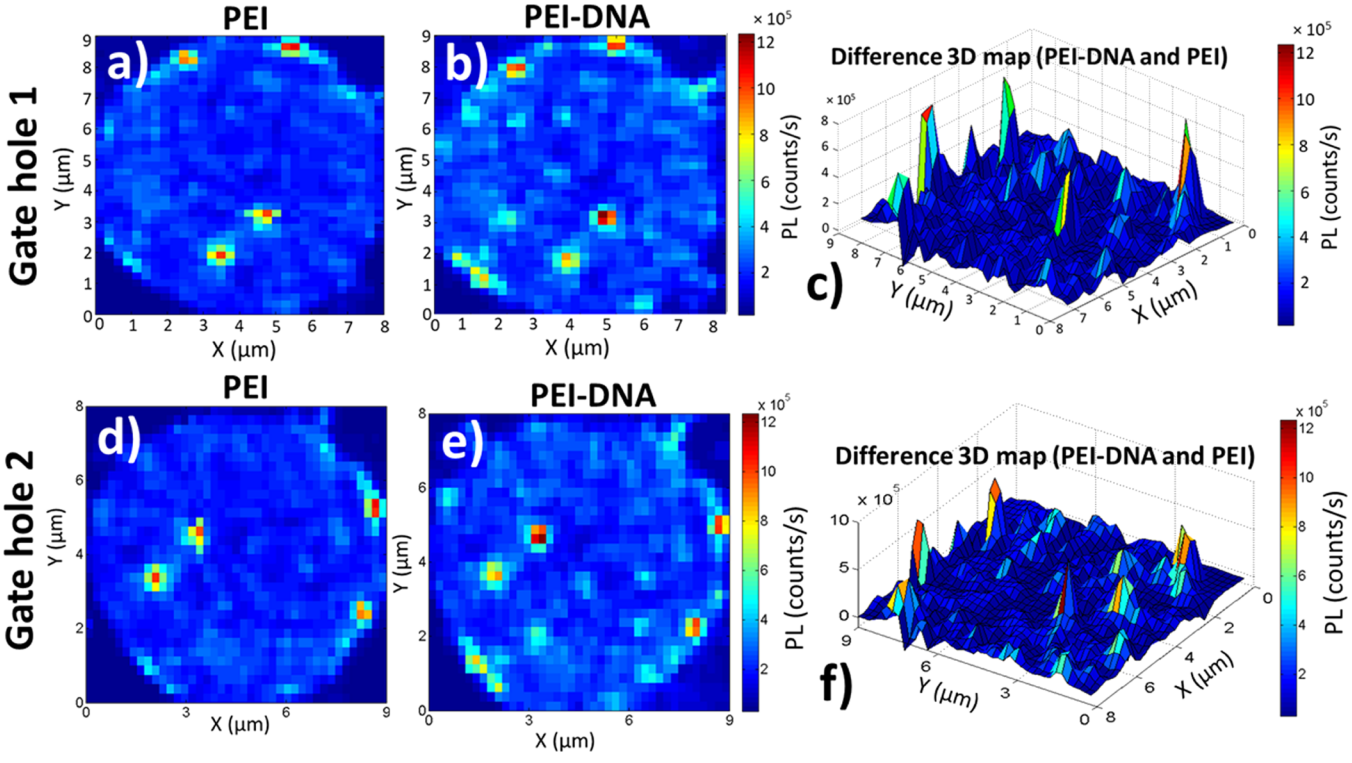

Figure 8. PL intensity maps measured on sample 2 in two different holes fabricated in the gate electrode, recorded with a long-pass spectral filter with cut-on wavelength at 650 nm to remove NV^0 PL. PL maps of the PEI functionalized diamond surface for (a) gate hole 1 and (d) gate hole 2 and PEI-DNA (100 μM) functionalized diamond surface for (b) gate hole 1 and (e) gate hole 2, monitored after complete attachment of the DNA to the surface. Corresponding 3D intensity difference maps of the PEI-DNA (100 μM) and PEI functionalized diamond surface for (c) gate hole 1 and (f) gate hole 2.

https://doi.org/10.1021/acsami.1c01118
ACS Appl. Mater. Interfaces 2021, 13, 18500−18510

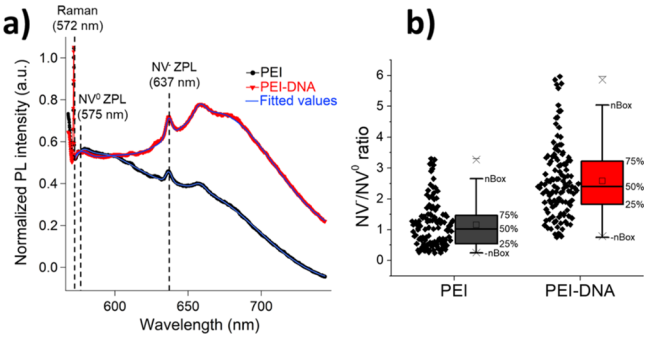

Figure 9. (a) Averaged NV PL spectra and (b) box chart of the NV^-/NV^0 ratio, calculated by fitting of spectra measured on sample 2 for PEI and PEI-DNA (100 μM) diamond surface functionalization at 123 different points on gate micro-holes (fitting with Lorentzian peaks representing NV^- and NV^0 PL - integrated intensity for ZPL and side bands). Spectra were normalized to the Raman line.

PEI-DNA complex. Despite the clear increase in the NV^--related PL intensity (see Figure 9a), the NV^0 PL intensity is almost unchanged, which could be attributed to conversion of dark NV^+ centers to NV^0. To provide statistics of NV^-/NV^0 ratio change with PEI and PEI-DNA functionalization, we fitted all individual spectra measured at 123 different positions. Figure 9b shows a box chart of the NV^-/NV^0 ratio calculated by Lorentzian peak fitting of NV^- and NV^0 PL, with an average value of 1.2 for PEI functionalization increasing to 2.6 (>2 times) after DNA attachment. These experimental results are consistent with band bending modeling (Figure 5; more details are in Supporting Information, Figure S5).

The observed difference in the NV^--related PL intensity after the immobilizations of DNA molecules with a concentration of 100 μM is ~500k counts. Considering the detection limit of ~500 counts on our setup, the detection limit is thus improved by a factor of 10 (i.e., about 100 nmol) compared to EIS for an estimated NV concentration of ~2 ppb corresponding to typically 10 NV centers in the confocal volume for the objective (N.A. = 0.8) used in our experiment. By increasing the NV center concentration to 1 ppm, this sensitivity limit could be further improved by a factor of 1000 (i.e., 100 pmol). Such an NV concentration would not affect significantly the band bending profile (for details, see calculations in Figure 5b and Figure S6 in the Supporting Information), and the Fermi level is still positioned below the NV^- GS level for PEI functionalization and above the NV^- GS level after DNA attachment and thus performance of the device is preserved. In addition, it is also possible to change the band bending and to set an optimal operational point of the device by applying a bias voltage on the gate electrode. Although we demonstrated the sensing concept for non-specific DNA attachment, detection of specific DNA and RNA molecules could be carried out by sensor surface hybridization with complementary ssDNA probes. It should be noted that our technique has sensitivity to just a single NV center, enabling, theoretically, detection of one or a few charged molecules placed within a very short distance from a single shallow NV, thus affecting its charge state. In addition, this technique can be further employed for the detection of the products of chemical reactions by active tuning of the Fermi level position to the electrochemical potential corresponding to the generation of such specific reaction products or combined with a nuclear or EPR spin detection.

4. CONCLUSIONS

In conclusion, we have fabricated a novel type of photoluminescence label-free diamond microfluidic DNA sensor based on the active control of NV center charge states with a possibility of setting up the electrochemical potential and by that to tune the detection to specific chemical reactions. The diamond detection chip contains boron-doped diamond (BDD) employed as an electrochemical electrode, also used for the verification of the sensing principle by measuring electrochemical impedance spectroscopy (EIS). By fabricating a thin (~20 nm) top layer of the un-doped diamond film with NV centers on top of the BDD, we were able to achieve a controlled percentage of negatively charged NV centers in the BDD-NV device. These NV centers are employed as sensitive electronic charge sensors. An active manipulation of the NV center charge state was accomplished by applying a bias voltage on the gate electrode fabricated on the diamond surface, switching the NV charge state between negative and neutral (or positive), and setting the operational point of the device. We fabricated a microfluidic device to flow DNA molecules over the diamond surface and employed this technique for label-free DNA sensing. DNA attachment was confirmed by electrochemical impedance spectroscopy, executed on the same device. After covering the diamond chip surface with a monolayer of strongly cationic charged polymer PEI, the charge state of the near surface NV centers was shown to become preferably NV^0 or NV^+. We demonstrated that upon electrostatic attachment of negative DNA molecules to positive PEI molecules, the intensity of NV^- photoluminescence strongly increases (by a factor of 2 in the case of a 100 μM DNA concentration) as the NV centers are being switched to the NV^- charge state. Time-dependent NV PL measurements during DNA bonding were performed and showed the fastest response for a maximum DNA concentration of 100 μM. For the utilized DNA molecules in solution, we estimated that this type of NV PL device could reach an optimal sensitivity of ~100 pmol by using 1 ppm NV-doped diamond. In future works, by applying voltage on the reference electrode, we plan to set the operational point of the device with respect to the electrochemical potential to sense the charged environment (such as species produced by electrochemical reactions) in various electrochemical systems. As we can detect photoluminescence from just one single NV center, this type of device could enable detection of one or a few charged molecules attached to the diamond surface above a shallow NV center. Also, although not explored in this work, further combination of the proposed device with NV NMR spin sensing would allow monitoring of changes of the spin environment in ongoing chemical reactions.

■ ASSOCIATED CONTENT

Supporting Information

The Supporting Information is available free of charge at https://pubs.acs.org/doi/10.1021/acsami.1c01118.

(Figure S1) Schemes of the two fabricated diamond chips: samples 1 and sample; (Figure S2) scheme of the diamond chip (sample 2) and microfluidic device connected to two electronic circuits; (Figure S3) band bending profile simulations of the oxygen-terminated surface of samples 1 and 2 in an electrolyte; (Figure S4) PL intensity 2D maps and differential 3D map of sample 1 with −3 and + 3 V gate voltages; band bending profile

https://doi.org/10.1021/acsami.1c01118
ACS Appl. Mater. Interfaces 2021, 13, 18500−18510

simulations of the oxygen-terminated surface of sample 1 immersed in an electrolyte with a higher nitrogen donor concentration of 10^{18} cm^{-3} in top layer at 0 V gate voltage and its NV^- center energy levels at applied gate voltages from -3 V to +3 V; (Figure S5) band bending simulation (sample 2, a nitrogen donor concentration of 10^{15} cm^{-3} in the top layer) for PEI and PEI-DNA surface functionalization at a 0 V gate voltage; NV^- center energy levels for PEI and PEI-DNA surface functionalization at a gate voltage from −1 to +3 V; (Figure S6) band bending simulation (sample 2, a nitrogen donor concentration of 10^{18} cm^{-3} in top layer) for PEI and PEI-DNA surface functionalization at a 0 V gate voltage; NV^- center energy levels for PEI and PEI-DNA surface functionalization at a gate voltage from −1 to +3 V; (Figure S7) comparison of NV PL spectra taken after 8 and 34 min for a DNA concentration of 10 μM during time-dependent DNA bonding on PEI-terminated diamond surfaces (sample 2); 2D map of micro-fabricated holes in the gate electrode; PL intensity maps measured on sample 2 in two different holes in the gate electrode for PEI and PEI-DNA functionalized diamond surfaces; and (Figure S8) scheme of an equivalent circuit used for EIS fitting; fitted parameters to the equivalent electrical circuit for investigation of sensor detection sensitivity with DNA concentrations ranging from 0 to 100 μM (sample 2) (PDF)

AUTHOR INFORMATION

Corresponding Author

Miloš Nesládek − *Department of Biomedical Technology, Faculty of Biomedical Engineering, Czech Technical University in Prague, 27201 Kladno, Czech Republic; IMOMEC division of MEC, B 3590 Diepenbeek, Belgium*; Phone: +32-11-268833; Email: milos.nesladek@uhasselt.be

Authors

Marie Krečmarová − *Department of Biomedical Technology, Faculty of Biomedical Engineering, Czech Technical University in Prague, 27201 Kladno, Czech Republic;* orcid.org/0000-0002-5401-5705

Michal Gulka − *Department of Biomedical Technology, Faculty of Biomedical Engineering, Czech Technical University in Prague, 27201 Kladno, Czech Republic; Institute for Materials Research, Material Physics Division University of Hasselt, B 3590 Diepenbeek, Belgium; Institute of Organic Chemistry and Biochemistry of the Czech Academy of Sciences, 166 10 Prague, Czechia*

Thijs Vandenryt − *Institute for Materials Research, Material Physics Division University of Hasselt, B 3590 Diepenbeek, Belgium; IMOMEC division of MEC, B 3590 Diepenbeek, Belgium;* orcid.org/0000-0001-8140-7221

Jaroslav Hrubý − *Institute for Materials Research, Material Physics Division University of Hasselt, B 3590 Diepenbeek, Belgium*

Ladislav Fekete − *FZU - Institute of Physics of the Czech Academy of Sciences, 182 21 Prague 8, Czech Republic*

Pavel Hubík − *FZU - Institute of Physics of the Czech Academy of Sciences, 182 21 Prague 8, Czech Republic*

Andrew Taylor − *FZU - Institute of Physics of the Czech Academy of Sciences, 182 21 Prague 8, Czech Republic*

Vincent Mortet − *Department of Biomedical Technology, Faculty of Biomedical Engineering, Czech Technical University in Prague, 27201 Kladno, Czech Republic; FZU - Institute of Physics of the Czech Academy of Sciences, 182 21 Prague 8, Czech Republic*

Ronald Thoelen − *Institute for Materials Research, Material Physics Division University of Hasselt, B 3590 Diepenbeek, Belgium; IMOMEC division of MEC, B 3590 Diepenbeek, Belgium*

Emilie Bourgeois − *Institute for Materials Research, Material Physics Division University of Hasselt, B 3590 Diepenbeek, Belgium; IMOMEC division of MEC, B 3590 Diepenbeek, Belgium*

Complete contact information is available at: https://pubs.acs.org/10.1021/acsami.1c01118

Author Contributions

M.N. conceptualized the study and provided work guidance; J.H. provided software; M.K., M.G., T.V., L.F., P.H., A.T., and E.B. conducted investigation; M.K. and M.G. conducted formal analysis; M.N., R.T., and V.M. provided resources; M.K. performed data curation; M.K. prepared the original draft; all co-authors reviewed and edited the manuscript; M.N., R.T., and V.M. acquired funding.

Funding

This research was funded by the [EU HORIZON Quantum Flagship Project ASTERIQS] grant number [820394], the [FWO (Flanders)] grant number [G.0.943.11.N.10.], the [CTU grant] grant number [SGS14/214/OHK4/3T/17], the [Czech Science Foundation (GACR)] grant numbers [GACR 16-16336S] and [GA20-28980S], the [SAFMAT] grant numbers [LM2015088] and [LO1409], the institutional resources of the Department of Biomedical Technology FBMI CTU, the Erasmus Student Mobility Grant, and the J. E. Purkyně fellowship awarded by the Academy of Sciences of the Czech Republic.

Notes

The authors declare no competing financial interest.

REFERENCES

(1) Badea, I.; Kaur, R. Nanodiamonds as Novel Nanomaterials for Biomedical Applications: Drug Delivery and Imaging Systems. *Int. J. Nanomed.* **2013**, *8*, 203−220.

(2) *Physics and Applications of CVD Diamond*; 1st ed.; Koizumi, S., Nebel, C., Nesladek, M., Eds.; Wiley: 2008. DOI: 10.1002/9783527623174.

(3) Vermeeren, V.; Wenmackers, S.; Wagner, P.; Michiels, L. DNA Sensors with Diamond as a Promising Alternative Transducer Material. *Sensors* **2009**, *9*, 5600−5636.

(4) Werner, M.; Locher, R.; Kohly, W.; Holmes, D. S.; Klose, S.; Fecht, H. J. The Diamond Irvin Curve. *Diamond Relat. Mater.* **1997**, *6*, 308−313.

(5) Gajewski, W.; Achatz, P.; Williams, O. A.; Haenen, K.; Bustarret, E.; Stutzmann, M.; Garrido, J. A. Electronic and Optical Properties of Boron-Doped Nanocrystalline Diamond Films. *Phys. Rev. B* **2009**, *79*, No. 045206.

(6) Fierro, S.; Mitani, N.; Comninellis, C.; Einaga, Y. PH Sensing Using Boron Doped Diamond Electrodes. *Phys. Chem. Chem. Phys.* **2011**, *13*, 16795.

(7) Bai, Y.-F.; Xu, T.-B.; Luong, J. H. T.; Cui, H.-F. Direct Electron Transfer of Glucose Oxidase-Boron Doped Diamond Interface: A New Solution for a Classical Problem. *Anal. Chem.* **2014**, *86*, 4910−4918.

(8) Gu, H.; Su, X. d.; Loh, K. P. Electrochemical Impedance Sensing of DNA Hybridization on Conducting Polymer Film-Modified Diamond. *J. Phys. Chem. B* **2005**, *109*, 13611−13618.
(9) Nidzworski, D.; Siuzdak, K.; Niedziałkowski, P.; Bogdanowicz, R.; Sobaszek, M.; Ryl, J.; Weiher, P.; Sawczak, M.; Wnuk, E.; Goddard, W. A., III; Jaramillo-Botero, A.; Ossowski, T. A Rapid-Response Ultrasensitive Biosensor for Influenza Virus Detection Using Antibody Modified Boron-Doped Diamond. *Sci. Rep.* **2017**, *7*, 15707.
(10) McDonald, M.; Monaco, A.; Vahidpour, F.; Haenen, K.; Giugliano, M.; Nesladek, M. Diamond Microelectrode Arrays for in Vitro Neuronal Recordings. *MRS Commun.* **2017**, *7*, 683−690.
(11) Doherty, M. W.; Manson, N. B.; Delaney, P.; Jelezko, F.; Wrachtrup, J.; Hollenberg, L. C. L. The Nitrogen-Vacancy Colour Centre in Diamond. *Phys. Rep.* **2013**, *528*, 1−45.
(12) Lagomarsino, S.; Gorelli, F.; Santoro, M.; Fabbri, N.; Hajeb, A.; Sciortino, S.; Palla, L.; Czelusniak, C.; Massi, M.; Taccetti, F.; Giuntini, L.; Gelli, N.; Fedyanin, D. Y.; Cataliotti, F. S.; Toninelli, C.; Agio, M. Robust Luminescence of the Silicon-Vacancy Center in Diamond at High Temperatures. *AIP Adv.* **2015**, *5*, 127117.
(13) Mamin, H. J.; Kim, M.; Sherwood, M. H.; Rettner, C. T.; Ohno, K.; Awschalom, D. D.; Rugar, D. Nanoscale Nuclear Magnetic Resonance with a Nitrogen-Vacancy Spin Sensor. *Science* **2013**, *339*, 557−560.
(14) Grotz, B.; Beck, J.; Neumann, P.; Naydenov, B.; Reuter, R.; Reinhard, F.; Jelezko, F.; Wrachtrup, J.; Schweinfurth, D.; Sarkar, B.; Hemmer, P. Sensing External Spins with Nitrogen-Vacancy Diamond. *New J. Phys.* **2011**, *13*, No. 055004.
(15) Shi, F.; Zhang, Q.; Wang, P.; Sun, H.; Wang, J.; Rong, X.; Chen, M.; Ju, C.; Reinhard, F.; Chen, H.; Wrachtrup, J.; Wang, J.; Du, J. Single-Protein Spin Resonance Spectroscopy under Ambient Conditions. *Science* **2015**, *347*, 1135−1138.
(16) Perunicic, V. S.; Hill, C. D.; Hall, L. T.; Hollenberg, L. C. L. A Quantum Spin-Probe Molecular Microscope. *Nat. Commun.* **2016**, *7*, 12667.
(17) Wrachtrup, J.; Finkler, A. Single Spin Magnetic Resonance. *J. Magn. Reson.* **2016**, *269*, 225−236.
(18) Balasubramanian, G.; Lazariev, A.; Arumugam, S. R.; Duan, D. Nitrogen-Vacancy Color Center in Diamond—Emerging Nanoscale Applications in Bioimaging and Biosensing. *Curr. Opin. Chem. Biol.* **2014**, *20*, 69−77.
(19) Staudacher, T.; Raatz, N.; Pezzagna, S.; Meijer, J.; Reinhard, F.; Meriles, C. A.; Wrachtrup, J. Probing Molecular Dynamics at the Nanoscale via an Individual Paramagnetic Centre. *Nat. Commun.* **2015**, *6*, 8527.
(20) Aslam, N.; Pfender, M.; Neumann, P.; Reuter, R.; Zappe, A.; Fávaro de Oliveira, F.; Denisenko, A.; Sumiya, H.; Onoda, S.; Isoya, J.; Wrachtrup, J. Nanoscale Nuclear Magnetic Resonance with Chemical Resolution. *Science* **2017**, *357*, 67−71.
(21) DeVience, S. J.; Pham, L. M.; Lovchinsky, I.; Sushkov, A. O.; Bar-Gill, N.; Belthangady, C.; Casola, F.; Corbett, M.; Zhang, H.; Lukin, M.; Park, H.; Yacoby, A.; Walsworth, R. L. Nanoscale NMR Spectroscopy and Imaging of Multiple Nuclear Species. *Nature Nanotech* **2015**, *10*, 129−134.
(22) Bourgeois, E.; Jarmola, A.; Siyushev, P.; Gulka, M.; Hruby, J.; Jelezko, F.; Budker, D.; Nesladek, M. Photoelectric Detection of Electron Spin Resonance of Nitrogen-Vacancy Centres in Diamond. *Nat. Commun.* **2015**, *6*, 8577.
(23) Bourgeois, E.; Gulka, M.; Nesladek, M. Photoelectric Detection and Quantum Readout of Nitrogen-Vacancy Center Spin States in Diamond. *Adv. Optical Mater.* **2020**, *8*, 1902132.
(24) Orwa, J. O.; Greentree, A. D.; Aharonovich, I.; Alves, A. D. C.; Van Donkelaar, J.; Stacey, A.; Prawer, S. Fabrication of Single Optical Centres in Diamond—a Review. *J. Lumin.* **2010**, *130*, 1646−1654.
(25) Schreyvogel, C.; Polyakov, V.; Wunderlich, R.; Meijer, J.; Nebel, C. E. Active Charge State Control of Single NV Centres in Diamond by In-Plane Al-Schottky Junctions. *Sci. Rep.* **2015**, *5*, 12160.
(26) Iakoubovskii, K.; Adriaenssens, G. J.; Nesládek, M.; Stals, L. M. Photoluminescence Excitation and Quenching Spectra in CVD Diamond Films. *Diamond Relat. Mater.* **1999**, *8*, 717−720.
(27) Petrakova, V.; Rehor, I.; Stursa, J.; Ledvina, M.; Nesladek, M.; Cigler, P. Charge-Sensitive Fluorescent Nanosensors Created from Nanodiamonds. *Nanoscale* **2015**, *7*, 12307−12311.
(28) Havlik, J.; Raabova, H.; Gulka, M.; Petrakova, V.; Krecmarova, M.; Masek, V.; Lousa, P.; Stursa, J.; Boyen, H.-G.; Nesladek, M.; Cigler, P. Benchtop Fluorination of Fluorescent Nanodiamonds on a Preparative Scale: Toward Unusually Hydrophilic Bright Particles. *Adv. Funct. Mater.* **2016**, *26*, 4134−4142.
(29) Petráková, V.; Nesládek, M.; Taylor, A.; Fendrych, F.; Cígler, P.; Ledvina, M.; Vacík, J.; Štursa, J.; Kučka, J. Luminescence Properties of Engineered Nitrogen Vacancy Centers in a Close Surface Proximity. *Phys. Status Solidi A* **2011**, *208*, 2051−2056.
(30) Hauf, M. V.; Grotz, B.; Naydenov, B.; Dankerl, M.; Pezzagna, S.; Meijer, J.; Jelezko, F.; Wrachtrup, J.; Stutzmann, M.; Reinhard, F.; Garrido, J. A. Chemical Control of the Charge State of Nitrogen-Vacancy Centers in Diamond. *Phys. Rev. B* **2011**, *83*, No. 081304.
(31) Grotz, B.; Hauf, M. V.; Dankerl, M.; Naydenov, B.; Pezzagna, S.; Meijer, J.; Jelezko, F.; Wrachtrup, J.; Stutzmann, M.; Reinhard, F.; Garrido, J. A. Charge State Manipulation of Qubits in Diamond. *Nat. Commun.* **2012**, *3*, 729.
(32) Kato, H.; Wolfer, M.; Schreyvogel, C.; Kunzer, M.; Müller-Sebert, W.; Obloh, H.; Yamasaki, S.; Nebel, C. Tunable Light Emission from Nitrogen-Vacancy Centers in Single Crystal Diamond PIN Diodes. *Appl. Phys. Lett.* **2013**, *102*, 151101.
(33) Doi, Y.; Makino, T.; Kato, H.; Takeuchi, D.; Ogura, M.; Okushi, H.; Morishita, H.; Tashima, T.; Miwa, S.; Yamasaki, S.; Neumann, P.; Wrachtrup, J.; Suzuki, Y.; Mizuochi, N. Deterministic Electrical Charge-State Initialization of Single Nitrogen-Vacancy Center in Diamond. *Phys. Rev. X* **2014**, *4*, No. 011057.
(34) Pfender, M.; Aslam, N.; Simon, P.; Antonov, D.; Thiering, G.; Burk, S.; Fávaro de Oliveira, F.; Denisenko, A.; Fedder, H.; Meijer, J.; Garrido, J. A.; Gali, A.; Teraji, T.; Isoya, J.; Doherty, M. W.; Alkauskas, A.; Gallo, A.; Grüneis, A.; Neumann, P.; Wrachtrup, J. Protecting a Diamond Quantum Memory by Charge State Control. *Nano Lett.* **2017**, *17*, 5931−5937.
(35) Hauf, M. V.; Simon, P.; Aslam, N.; Pfender, M.; Neumann, P.; Pezzagna, S.; Meijer, J.; Wrachtrup, J.; Stutzmann, M.; Reinhard, F.; Garrido, J. A. Addressing Single Nitrogen-Vacancy Centers in Diamond with Transparent in-Plane Gate Structures. *Nano Lett.* **2014**, *14*, 2359−2364.
(36) Karaveli, S.; Gaathon, O.; Wolcott, A.; Sakakibara, R.; Shemesh, O. A.; Peterka, D. S.; Boyden, E. S.; Owen, J. S.; Yuste, R.; Englund, D. Modulation of Nitrogen Vacancy Charge State and Fluorescence in Nanodiamonds Using Electrochemical Potential. *Proc. Natl. Acad. Sci. U. S. A.* **2016**, *113*, 3938−3943.
(37) Petrakova, V.; Benson, V.; Buncek, M.; Fiserova, A.; Ledvina, M.; Stursa, J.; Cigler, P.; Nesladek, M. Imaging of Transfection and Intracellular Release of Intact, Non-Labeled DNA Using Fluorescent Nanodiamonds. *Nanoscale* **2016**, *8*, 12002−12012.
(38) Krečmarová, M.; Vandenryt, T.; Gulka, M.; Bourgeois, E.; Fekete, L.; Hubík, P.; Thoelen, R.; Mortet, V.; Nesládek, M. Microfluidic Diamond Biosensor Using NV Centre Charge State Detection. In *World Congress on Medical Physics and Biomedical Engineering 2018*; Lhotska, L., Sukupova, L., Lacković, I., Ibbott, G. S., Eds.; IFMBE Proceedings; Springer Singapore: Singapore, 2019; Vol. *68/3*, pp. 27−31. DOI: 10.1007/978-981-10-9023-3_6.
(39) Macpherson, J. V. A Practical Guide to Using Boron Doped Diamond in Electrochemical Research. *Phys. Chem. Chem. Phys.* **2015**, *17*, 2935−2949.
(40) MathWorks. *Matlab Software*; MathWorks: Https://Www.Mathworks.Com/Products/Matlab.Html.
(41) Rondin, L.; Dantelle, G.; Slablab, A.; Grosshans, F.; Treussart, F.; Bergonzo, P.; Perruchas, S.; Gacoin, T.; Chaigneau, M.; Chang, H.-C.; Jacques, V.; Roch, J.-F. Surface-Induced Charge State Conversion of Nitrogen-Vacancy Defects in Nanodiamonds. *Phys. Rev. B* **2010**, *82*, 115449.

(42) *AMPS-1D Analysis of Microelectronic and Photonic Structures*; AMPS: Http://Www.Ampsmodeling.Org/Default.Htm.
(43) Scribner Associates. *Zview Software*; Scribner Associates, Inc.: Http://Www.Scribner.Com/Software/.
(44) Petráková, V.; Taylor, A.; Kratochvílová, I.; Fendrych, F.; Vacík, J.; Kučka, J.; Štursa, J.; Cígler, P.; Ledvina, M.; Fišerová, A.; Kneppo, P.; Nesládek, M. Luminescence of Nanodiamond Driven by Atomic Functionalization: Towards Novel Detection Principles. *Adv. Funct. Mater.* **2012**, *22*, 812−819.
(45) Krysova, H.; Vlckova-Zivcova, Z.; Barton, J.; Petrak, V.; Nesladek, M.; Cigler, P.; Kavan, L. Visible-Light Sensitization of Boron-Doped Nanocrystalline Diamond through Non-Covalent Surface Modification. *Phys. Chem. Chem. Phys.* **2015**, *17*, 1165−1172.
(46) Long, Y.-T.; Li, C.-Z.; Kraatz, H.-B.; Lee, J. S. AC Impedance Spectroscopy of Native DNA and M-DNA. *Biophys. J.* **2003**, *84*, 3218−3225.
(47) Pänke, O.; Balkenhohl, T.; Kafka, J.; Schäfer, D.; Lisdat, F. Impedance Spectroscopy and Biosensing. In *Biosensing for the 21st Century*; Renneberg, R., Lisdat, F., Eds.; Advances in Biochemical Engineering/Biotechnology; Springer Berlin Heidelberg: Berlin, Heidelberg, 2008; Vol. *109*, pp. 195−237. DOI: 10.1007/10_2007_081.

https://doi.org/10.1021/acsami.1c01118
ACS Appl. Mater. Interfaces 2021, 13, 18500−18510